Optoelectronic properties and depth profile of charge transport in nanocrystal films

Willi Aigner,[1] Oliver Bienek,[1] Derese Desta,[2] Hartmut Wiggers,[3] Martin Stutzmann,[1] and Rui N. Pereira[1,2,*]

[1]*Walter Schottky Institut and Physik-Department, Technische Universität München, Am Coulombwall 4, 85748 Garching, Germany*

[2]*Department of Physics and I3N, University of Aveiro, 3810-193 Aveiro, Portugal*

[3]*Institute for Combustion and Gasdynamics-Reactive Fluids-and CENIDE, Center for Nanointegration Duisburg-Essen, Universität Duisburg-Essen, Carl-Benz-Straße 199, 47057 Duisburg, Germany*

(Received 9 March 2017; revised manuscript received 8 May 2017; published 5 July 2017)

We investigate the charge transport in nanocrystal (NC) films using field effect transistors (FETs) of silicon NCs. By studying films with various thicknesses in the dark and under illumination with photons with different penetration depths (UV and red light), we are able to predictably change the spatial distribution of charge carriers across the films' profile. The experimental data are compared with photoinduced charge carrier generation rates computed using finite-difference time-domain (FDTD) simulations complemented with optical measurements. This enables us to understand the optoelectronic properties of NC films and the depth profile dependence of the charge transport properties. From electrical measurements, we extract the total (bulk) photoinduced charge carrier densities (n_{photo}) and the photoinduced charge carrier densities in the FETs channel (n^*_{photo}). We observe that the values of n_{photo} and their dependence on film thickness are similar for UV and red light illumination, whereas a significant difference is observed for the values of n^*_{photo}. The dependencies of n_{photo} and n^*_{photo} on film thickness and illumination wavelength are compared with data from FDTD simulations. Combining experimental data and simulation results, we find that charge carriers in the top rough surface of the films cannot contribute to the macroscopic charge transport. Moreover, we conclude that below the top rough surface of NC films, the efficiency of charge transport, including the charge carrier mobility, is homogeneous across the film thickness. Our work shows that the use of NC films as photoactive layers in applications requiring harvesting of strongly absorbed photons such as photodetectors and photovoltaics demands a very rigorous control over the films' roughness.

DOI: 10.1103/PhysRevB.96.035404

I. INTRODUCTION

Thin films of semiconducting nanocrystals (NCs) are attracting a great deal of attention for application in novel electronic and optoelectronic devices [1–10]. High-quality semiconductor NCs can now be synthesized with high yield using many different solution- and gas-phase techniques [6,11–15], providing a huge flexility in terms of device fabrication. Thin films of NCs can be deposited with high deposition rates by means of printing-type techniques, such as inkjet printing and spray coating, using liquid dispersions of NCs (nanocrystal inks). This enables a cost-efficient bottom-up assembling of NC films over large areas onto temperature-sensitive substrates, e.g., flexible plastics and textiles [16,17], unlike conventional higher-temperature and more costly vacuum deposition methods. Moreover, the tunability of the optical and electronic properties of the individual NC building blocks via control of their composition, size, shape, surface chemistry, and doping represents a great opportunity to fabricating unprecedented (opto)electronic devices [1–3].

Charge transport is fundamental in all envisaged applications of NC films. However, the nature of charge transport in NC films is still under intense debate [3,18]. In particular, a better understanding of the transport of photogenerated charges in NCs is required to optimize the application of these materials in optoelectronic devices such as photodetectors [19–21] and photovoltaics [22–31]. The optoelectronic properties of NC films have only been addressed in regard to the tunability of the NC energy band gap and the NCs absorption coefficient [3,32]. Moreover, due to the large surface-to-volume ratio of NCs, the transport of charges depends on the surface properties of the NCs and on the interface between neighboring NCs [3,18,33]. Also, the morphology of the films plays an important role in transport due to percolation effects [3,34–37]. However, the impact of the morphology of NC films on their optoelectronic properties has not been studied systematically. Moreover, the contribution of charge transport in different portions of a NC film across its thickness is also not well understood.

In this work, we use Si NC field effect transistors (FETs) to study the transport of photogenerated charge carriers in NC films. We compare the charge transport of the NC devices in the dark and under illumination with UV ($\lambda = 390$ nm) and red ($\lambda = 623$ nm) light. Using films with various thicknesses and light with significantly different penetration depths (UV and red light), we are able to tune the spatial distribution of photoinduced charge carriers across the films' profile and probe different portions of the NC films. In this way, we determine the photoinduced charge carrier density in the total (bulk) film and the photoinduced charge carrier density in the FET channel as a function of the NC film thickness. The photoinduced charge carrier density in the bulk film is obtained from comparing conductivity/mobility ratios in the dark and under illumination and the photoinduced charge carrier density in the channel is obtained from comparing FET threshold voltages in the dark and under illumination. Finite-difference time-domain (FDTD) simulations of the Si NC FETs under illumination are carried out to compute the generation rates

*pereira@wsi.tum.de; rnpereira@ua.pt

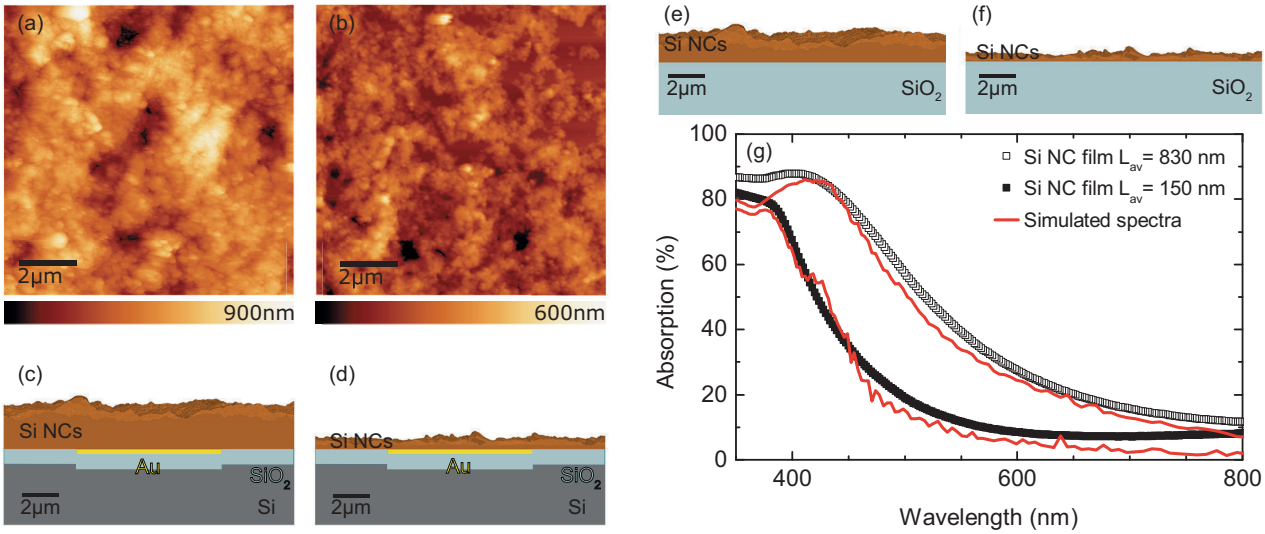

FIG. 1. AFM micrographs of Si NC films with (a) $L = 700$ nm and (b) $L = 60$ nm. The AFM micrographs are used to build up a simulation model of Si NC films on 130 nm Au and 300 nm silicon oxide on (c), (d) a silicon wafer and on (e), (f) quartz glass. (g) Optical absorption data of Si NC films on quartz glass with $L_{av} = 830$ nm (open squares) and $L_{av} = 150$ nm (full squares) and simulated spectra (red lines) using the models in (e) and (f).

of charge carriers, which are compared with the experimental photoinduced charge carrier densities.

II. METHODS

A. Experimental methods

Si NCs are synthesized in a low-pressure flow reactor by microwave-induced decomposition of silane [38]. In this work, we use nominally undoped Si NCs with a mean diameter $d_{\text{as grown}} \approx 20$ nm that are covered with a native oxide shell [39]. Si NC films are prepared by spray coating a Si NC ink consisting of H-terminated Si NCs (1 wt. %) in chlorobenzene. To this end, the as-grown Si NCs are immersed in HF (10% vol in H_2O) to remove the oxide shell and render the Si NCs H-terminated. The Si NC ink is deposited using a homemade spray-coating setup yielding homogeneous Si NC films with a tunable film thickness. Bottom-gate Si NC FETs are fabricated on highly p-type doped Si substrates covered with a 300 nm silicon oxide dielectric layer. The substrates are patterned with interdigit contact structures (130 nm Au, 50 fingers, length 1.88 mm, spacing 20 μm) fabricated by means of photolithography and thermal evaporation. For optical absorption measurements, quartz glass substrates are used. A more detailed description of the HF etching, the Si NC ink formation, and the spray-coating process is published elsewhere [34].

The Si NC film thickness is measured using a DekTak 150 surface profiler with a stylus diameter of 12.5 μm. The surface exhibits a typical roughness of 100–200 nm. We define the effective film thickness L as the lower 5 percentile of the film thickness where a continuous coverage with NCs is ensured (see Fig. 7) [34]. The average film thickness L_{av} is used for the analysis of optical absorption data. Atomic force microscopy (AFM) micrographs are recorded in Peak Force mode using a MultiMode 8 AFM System (Bruker). Optical absorption measurements are carried out employing a Perkin Elmer Lambda 900 spectrometer equipped with an integrating sphere to account for scattered light. For electrical measurements, a homemade needle station setup connected to a Keithley 2600 dual-channel source meter unit is used. To avoid reoxidation of the samples, the electrical measurements are carried out in an Ar-purged glovebox with O_2 and H_2O level below 1 ppm. The samples are illuminated with a 10-W UV LED ($\lambda = 390$ nm) and a 3-W red LED ($\lambda = 623$ nm) that are mounted next to the sample holder. Two sets of samples were prepared using similar deposition conditions. The illumination intensities are determined to be 7 mW/cm^2 ($\lambda = 390$ nm) and 13 mW/cm^2 ($\lambda = 623$ nm) for sample series I and 14 mW/cm^2 ($\lambda = 390$ nm) and 11 mW/cm^2 ($\lambda = 623$ nm) for sample series II. We measure current-voltage ($I - U$) characteristics with floating gate and transistor transfer curves (drain-source current I_{DS} versus gate voltage U_G) with a fixed drain-source voltage U_{DS} in darkness and under illumination.

B. FDTD simulations

Numerical calculations of optical absorption are carried out using a finite-difference time-domain (FDTD) simulation tool from Lumerical [40] to map the absorbed light in the Si NC films. We employ AFM micrographs of two samples with different film thickness ($L = 700 \pm 100$ nm and $L = 60 \pm 10$ nm) shown in Figs. 1(a) and 1(b). These AFM data are used to model the surface morphology (10 μm $\times$ 10 μm unit cell) of the Si NC FETs [Figs. 1(c) and 1(d)]. A Si wafer covered with a 300-nm-thick silicon dioxide and a 5 μm $\times$ 10 μm buried 130-nm-thick Au contact is considered as a substrate. The optical constants for the bulk Si wafer, the silicon dioxide, and the Au contact are taken from Palik's Handbook of optical constants [41]. The optical constants of the Si NC films differ from bulk Si values as the films exhibit lower densities due to their nanostructured, porous structure. To account for that, we compute the absorption spectrum of Si NC films on quartz glass [see Figs. 1(e) and 1(f)]. The

experimental optical absorbance A in Fig. 1(g) is obtained measuring the transmittance T and the reflectance R of the Si NC films with average film thicknesses $L_{av} = 830$ and 150 nm and using the relation $A = 100\,\% - R - T$. We find a strong increase of absorption with decreasing wavelength and increasing film thickness. To simulate these spectra, we apply the volume averaging theory (VAT) to adjust the optical constants of our porous Si NC films. Using the VAT model from Garahan [42], the optical constants of a NC film can be expressed as the effective refraction index n_{eff} and the effective absorption constant k_{eff}

$$n_{\text{eff}} = \tfrac{1}{2}[\alpha + \sqrt{\alpha^2 + \beta^2}], \tag{1a}$$

$$k_{\text{eff}} = \tfrac{1}{2}[-\alpha + \sqrt{\alpha^2 + \beta^2}] \tag{1b}$$

with

$$\alpha = \phi\left(n_{\text{air}}^2 - k_{\text{air}}^2\right) + (1-\phi)\left(n_{\text{Si}}^2 - k_{\text{Si}}^2\right), \tag{2a}$$

$$\beta = 2n_{\text{air}}k_{\text{air}}\phi + 2n_{\text{Si}}k_{\text{Si}}(1-\phi), \tag{2b}$$

where n_{air} is the refraction index of air (equal to one), k_{air} is the absorption index of air (equal to zero), n_{Si} and k_{Si} are the refraction and absorption indexes of bulk Si [41], and ϕ is the porosity factor in the VAT model. We find that using $\phi = 0.8$, the calculated spectra well represent the experimental data [see Fig. 1(g)]. The corresponding values of n_{eff} and k_{eff} are further used for simulations of the Si NC FETs. We note that at the large wavelengths, the experimental absorption is somewhat higher compared to the simulated values. This may be due to an underestimation of the diffused reflection in the measurements.

For the Si NC FETs, we map the photon absorption probability in two different cases: (i) absorption only within the effective film thickness L, and thus the photon absorption in the top rough surface of the film is neglected, and (ii) absorption only within the FET channel, considering a thickness of 50 nm for the latter. To allow a comparison with experimental data, we divide the absorption probability by the volume of the Si NC layer (film thickness L or channel thickness) and multiply it with the incoming photon flux, giving the charge carrier generation rate. The results of the simulations as a function of wavelength are shown in the Supplemental Material [43]. In the main text, we will focus mainly on the generation rate for $\lambda = 390$ and 623 nm computed for different, representative NC film thicknesses of $L = 60$, 250, 400, and 700 nm.

III. EXPERIMENTAL DATA

A. Si NC FETs under illumination

Figure 2(a) shows typical $I - U$ characteristics (floating gate) of Si NC FETs with two different thicknesses ($L = 60 \pm 15$ and 680 ± 90 nm) in darkness and under illumination with red and UV light. We find an increase of the current under illumination, which is more pronounced for the thinner film. For all data, the $I - U$ dependence is nonlinear at high voltages. This effect is explained by a space-charge-limited current transport mechanism giving rise to a linear $I - U$ dependence at low voltages and a power-law dependence at high voltages [34,39,44]

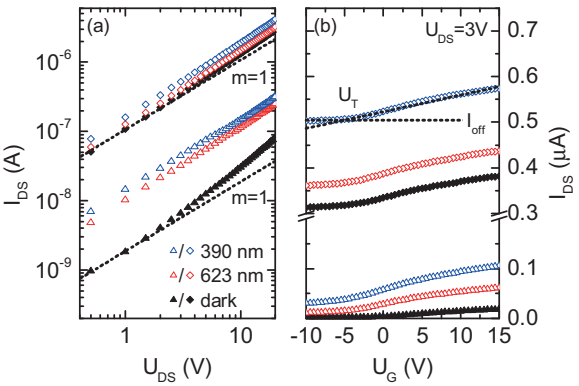

FIG. 2. (a) $I - U$ characteristics and (b) transfer curves of Si NC FETs with $L = 60 \pm 15$ nm (triangles) and $L = 680 \pm 90$ nm (diamonds) taken in darkness (black) and under illumination with $\lambda = 390$ nm (blue) and $\lambda = 623$ nm (red).

$$I = aU + bU^m, \tag{3}$$

where a, b, and m are parameters adjusted to fit the data. In this work, we focus on the low-voltage regime, where a corresponds to the Ohmic conductance G, which is used to calculate the electrical conductivity σ of the Si NC films.

Figure 2(b) shows transfer curves of the Si NC FETs in darkness and under illumination (I_{DS} versus U_{G}, $U_{\text{DS}} = 3$ V). For all data, we find a linear increase of current at positive gate voltages, which can be explained by an accumulation of electrons in the FET channel [34]. The current increases under illumination. To extract the field effect mobility μ and the threshold voltage U_{T}, we fit $I_{\text{DS}} - I_{\text{off}}$ using

$$(I_{\text{DS}} - I_{\text{off}}) \cong \frac{WC_i}{S}\mu(U_{\text{G}} - U_{\text{T}})U_{\text{DS}}, \tag{4}$$

where I_{off} is the current flowing when the FET channel is switched off [see Fig. 2(b)], W is the transistor channel width, C_i is the specific capacitance per area, and S is the electrode spacing [45]. In the fits, the value of I_{off} corresponds to the lowest value of current measured in the transfer curves. This equation is valid for small U_{DS} with $U_{\text{DS}} \ll (U_{\text{G}} - U_{\text{T}})$.

In Fig. 3, the conductance [panels (a) and (b)], the conductivity [panels (c) and (d)], and the field effect mobility [panels (e) and (f)] are plotted as a function of film thickness for sample series I [panels (a), (c), and (e)] and sample series II [panels (b), (d), and (f)]. Measurements are performed in darkness (black) and under illumination with UV light (blue) and red light (red). The conductance G increases monotonically with film thickness for both sets of data, in darkness and under illumination. We find that for thin films, the conductance under illumination is almost one order of magnitude higher than in darkness. For thicker films, the dark conductance approaches the conductance under illumination.

Using the conductance and the film thickness, we calculate the conductivity σ of the Si NC FETs [Figs. 3(c) and 3(d)]. We find that σ in darkness is fairly constant [Fig. 3(c)] or only

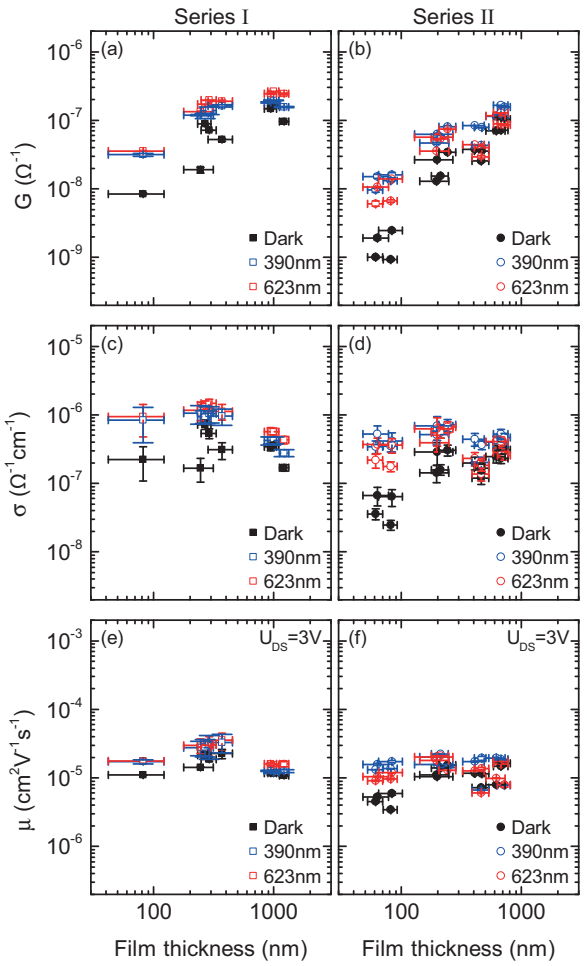

FIG. 3. (a), (b) Conductance G, (c), (d) conductivity σ, and (e), (f) mobility μ of Si NC FETs measured in darkness (black) and under illumination with $\lambda = 390$ nm (blue) and $\lambda = 623$ nm (red). The illumination intensities are determined to be 7 mW/cm^2 ($\lambda = 390$ nm) and 13 mW/cm^2 ($\lambda = 623$ nm) for sample series I (square symbols) and 14 mW/cm^2 ($\lambda = 390$ nm) and 11 mW/cm^2 ($\lambda = 623$ nm) for sample series II (circle symbols).

exhibits a small increase with film thickness [Fig. 3(d)] with values around 10^{-7} Ω^{-1}cm^{-1}. This result is different from our previous report where a strong dependence on the film thickness has been reported [34] and will be further discussed below. The conductivity under illumination is about one order of magnitude higher for thin films and approaches dark values for larger film thicknesses. Interestingly, we do not observe a significant difference in photoconductivity under UV and red illumination, although the optical absorption for the two wavelengths is very different [see Fig. 1(g)].

The field effect mobility in darkness [Figs. 3(e) and 3(f)] is around 10^{-5} cm^2 V^{-1} s^{-1}, almost independent of film thickness. We assume that the FET channel is much thinner than the film thickness and, therefore, does not depend on L, which agrees with the literature (channel thickness ≈50 nm) [34,46]. Under red and UV illumination, we find a small increase of the field effect mobility with respect to the dark values. This increase is up to a factor of 3 for thin Si NC

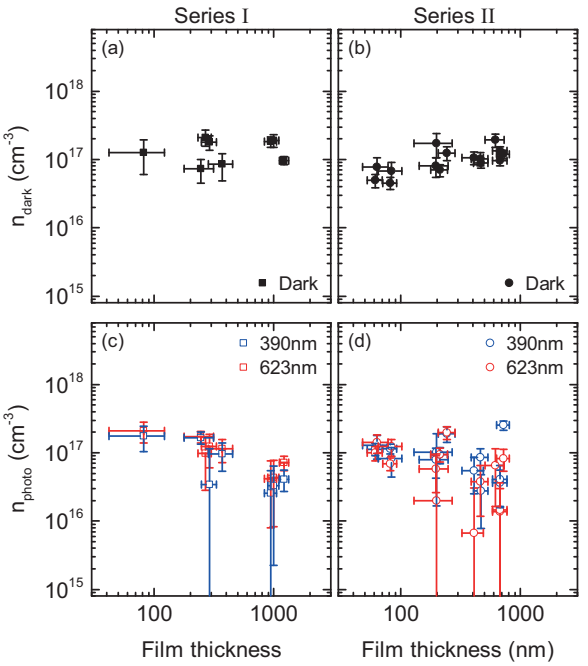

FIG. 4. (a), (b) Charge carrier density in darkness n_{dark} calculated using Eq. (5). (c), (d) Photoinduced charge carrier density n_{photo} for $\lambda = 390$ nm (blue) and $\lambda = 623$ nm (red).

FETs and, in principle, can be interpreted as a photoenhanced mobility, which will be discussed below.

We use the dark conductivity σ_{dark} and dark field effect mobility values μ_{dark} to calculate the charge carrier density in darkness n_{dark}, assuming that the mobility is constant throughout the electrically active volume of the Si NC films and using the relation

$$n_{\text{dark}} = \sigma_{\text{dark}}/(e\mu_{\text{dark}}), \tag{5}$$

where e is the elementary charge [45]. In Figs. 4(a) and 4(b), we find that n_{dark} does not significantly depend on the film thickness and scatters around 10^{17} cm^{-3}. In a previous study, we have reported that the values given by Eq. (5) strongly increase on the film thickness and explained the increase with percolation effects [34]. In such a case, Eq. (5) gives only an apparent charge carrier density instead of n_{dark}. The fact that the values of n_{dark} shown in Figs. 4(a) and 4(b) are mostly independent of film thickness indicates that for the present films percolation effects are unimportant and, therefore, Eq. (5) gives the charge carrier density in the dark n_{dark}. We conclude that the difference between the observations in the two studies is due to different substrates used for the Si NC FETs (Si wafers covered with SiO_2 in this study and covered with Si_3N_4 in the previous work). To confirm the influence of the substrate, we have deposited Si NCs used for the current study on substrates covered with Si_3N_4 and carried out measurements of n_{dark}. These data are shown in the Supplemental Material [43]. We find a clear increase of n_{dark} with film thickness in accordance with the previous study. We suggest that the wetting properties on the two dielectric materials with the Si NC ink differ and may lead to a different morphology of the Si NC films, which determines the formation of percolation paths. In the case of

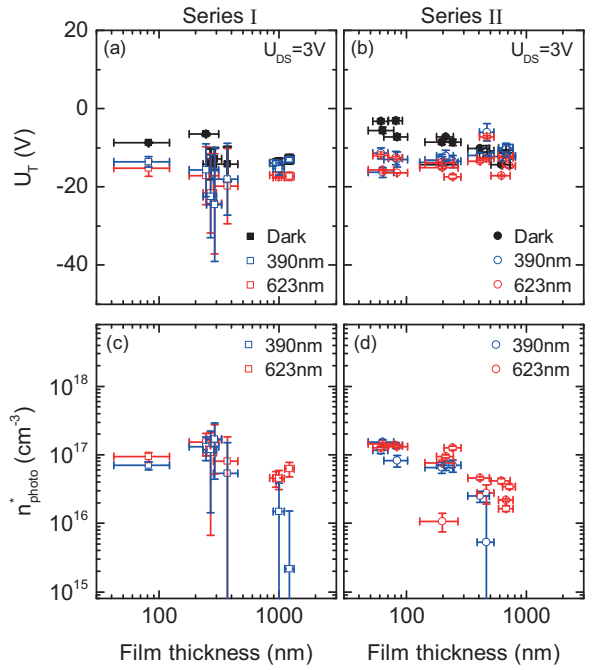

FIG. 5. (a), (b) Threshold voltage U_T taken at $U_{DS} = 3$ V measured in darkness (black) and under illumination with $\lambda = 390$ nm (blue) and $\lambda = 623$ nm (red). (c), (d) Photoinduced charge carrier density calculated using Eq. (8) and the data in (a) and (b).

SiO_2 as a dielectric, the Si NCs may form denser layers at low film thicknesses.

B. Photogenerated charge carrier density

The photoinduced charge carrier density is calculated using

$$n_{\text{photo}} = \sigma_{\text{illu}}/(e\mu_{\text{illu}}) - n_{\text{dark}}, \tag{6}$$

where σ_{illu} and μ_{illu} are the conductivity and field effect mobility obtained under illumination. The values of n_{photo} are shown in Figs. 4(c) and 4(d). For both sets of data, n_{photo} is about 10^{17} cm^{-3}, which is comparable to n_{dark}. With increasing film thickness, we find a slight decrease of n_{photo}, which is on average about 0.5 orders of magnitude for both UV and red light illumination.

In Figs. 5(a) and 5(b), the threshold voltages of the NC FETs in darkness (black) and under UV and red light illumination (blue and red) are shown as a function of film thickness. In darkness, U_T is constant or slightly decreases with L, exhibiting mean values around -10 V. Under illumination, U_T tends to become more negative. This is more pronounced for thin films. The threshold voltage in the accumulation regime is a function of the charge carrier density n^* in the FET channel

$$U_T = U_{FB} - \frac{eln^*}{C_i}, \tag{7}$$

where U_{FB} is the flat band voltage, e is the elementary charge, and l is the thickness for the channel. Here, we assume the value of $l = 50$ nm following recent studies [46] and consistent with values considered in our previous investigation [34]. We note that in the case of nanoparticle films, it is reasonable to consider that l is larger than the NCs diameter ($\sim$20 nm).

We extract the difference between the threshold voltage in darkness $U_{T\,\text{dark}}$ and under illumination $U_{T\,\text{illu}}$ to calculate the photoinduced charge carrier density in the FET channel n^*_{photo} using

$$n^*_{\text{photo}} = n^*_{\text{illu}} - n^*_{\text{dark}} = (U_{T\,\text{dark}} - U_{T\,\text{illu}}) \times \frac{C_i}{el}; \tag{8}$$

n^*_{photo} is plotted in Figs. 5(c) and 5(d). We note also that the value of l used here should not have a significant impact in our discussion because it is not focused in the absolute values of n^*_{photo}. Under UV light, n^*_{photo} decreases from 10^{17} cm^{-3} for thin Si NC FETs to values two orders of magnitude lower for μm-thick Si NC FETs. In Fig. 5(d), n^*_{photo} of the thickest Si NC FETs is below the detection limit as the difference between the respective threshold voltages is very small. Under red light illumination, n^*_{photo} shows similar values for thin Si NC FETs ($\approx 10^{17}$ cm^{-3}), but exhibits a smaller decrease of less than one order of magnitude with increasing film thickness.

C. Time-resolved and intensity-dependent photocurrent

Aside from the steady-state charge carrier densities, the dynamics and the intensity dependence of the photocurrent are important to check for temperature effects and characterize the recombination mechanism present in the Si NC films. In Fig. 6(a), the time dependence of the current measured at a fixed voltage ($U_{DS} = 10$ V) is shown in darkness and under illumination with UV light for thin [$L = (130 \pm 30)$ nm] and thick [$L = (1140 \pm 80)$ nm] Si NC films. We find that upon illumination, there is an immediate jump in the current as well as a small further increase with a longer time constant. Taking into account the long time scales of the current rise (as well as of its decay), we can speculate that this is due to a slow heating of the NCs due to thermalization of photoinduced

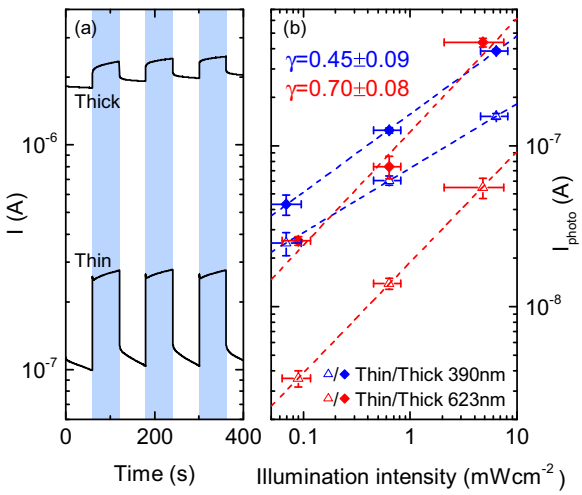

FIG. 6. (a) Current taken at $U_{DS} = 10$ V as a function of time for a thin Si NC film ($L = 130 \pm 30$ nm) and a thick Si NC film ($L = 1140 \pm 80$ nm). Blue-shaded areas represent illumination with UV light (6 ± 2 mWcm^{-2}). (b) Photocurrent of the thin and thick Si NC films in (a) with different illumination intensities for $\lambda = 390$ nm (blue) and $\lambda = 623$ nm (red). Dashed lines are a fit to the data using Eq. (9).

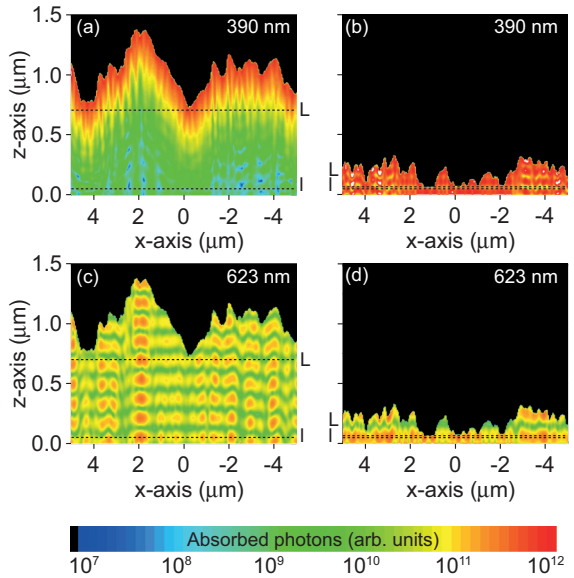

FIG. 7. Optical absorption profile of Si NC films on FET structures illustrated in Fig. 1 with (a), (c) film thicknesses $L =$ 700 nm and (b), (d) $L = 60$ nm for (a), (b) $\lambda = 390$ nm and (c), (d) $\lambda = 623$ nm.

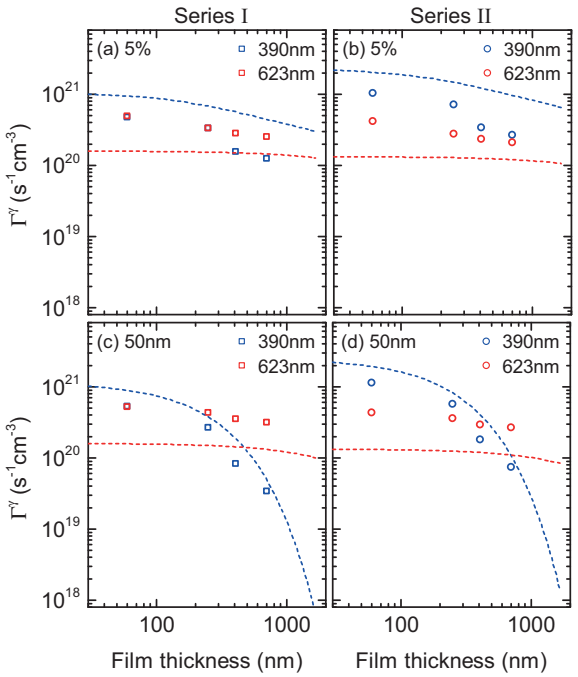

FIG. 8. Calculated charge carrier generation rates in Si NC films (see Figs. 1 and 7) for $\lambda = 390$ nm (blue circles) and $\lambda = 623$ nm (red circles). (a), (b) Generation rates in the 5 percentile thickness L of the Si NC films, (c), (d) generation rates in the lower 50nm of the Si NC films (FET channel). Dashed lines are calculated using the Lambert-Beer law.

charge carriers. The absolute value of the sudden increase is referred to as the photocurrent (I_{photo}).

In Fig. 6(b), I_{photo} is plotted as a function of the illumination intensity. The scaling of the photocurrent depends on the predominant recombination mechanism. In the literature, this is done via a power-law dependence

$$I_{\text{photo}} \propto F^{\gamma}, \tag{9}$$

where F is the illumination intensity and γ is a power-law coefficient [47]. Our data show a sublinear increase with intensity. The thin and thick Si NC film samples exhibit a similar scaling under UV and red light illumination, suggesting that the recombination mechanism is similar throughout the film. Fitting the data using Eq. (9), we find $\gamma = (0.45 \pm 0.09)$ for 390 nm and $\gamma = (0.70 \pm 0.08)$ for 623 nm. In the literature, $\gamma = 1$ is attributed to a monomolecular recombination process with a high concentration of recombination centers near the dark Fermi level [48]. A value $\gamma \approx 0.5$ suggests a bimolecular recombination process typically observed for band-to-band recombination. Trap states may also influence the recombination process [39,48]. A power-law dependence of $0.5 \leqslant \gamma \leqslant 1$ is expected for photoconductors with both deep recombination centers and a distribution of trap states [48]. For Si NC films, $\gamma \approx 0.6$ is reported for measurements in air using white-light illumination [39]. This value is between our measured data for UV and red light. We consider that the wavelength dependence of γ observed in this study is a sign that the recombination shifts from a mechanism involving deep recombination centers and a distribution of trap states for red illumination to a more bimolecular recombination mechanism for UV illumination.

IV. SIMULATION RESULTS

To investigate the nature of the observed different scaling of n_{photo} and n^{*}_{photo} with film thickness, FDTD simulations are carried out to compute the absorption of light in the Si NC FETs. The models for the calculation are shown in Figs. 1(c) and 1(d). We obtain optical absorption profiles of the NC films under illumination (UV and red light) for different film thicknesses, which are plotted in Fig. 7. Under UV illumination [Figs. 7(a) and 7(b)], the absorption is high at the top interface of the Si NC films and significantly decreases at low-z values. If the Si NC film is thin [Fig. 7(b)], the absorption is almost constant within the entire film. When illuminated with red light [Figs. 7(c) and 7(d)], we find interference effects leading to an oscillation around some mean absorption value that is constant across the entire film. This is the same for thick and thin Si NC films. We evaluate the simulated absorption profiles integrating the amount of absorbed photos up to $z = L$ and up to $z = l = 50$ nm. The data are shown as a function of wavelength in the Supplemental Material [43]. Using this computed absorption probability P, we calculate the generation rate of charge carriers Γ:

$$\Gamma = \frac{P}{V} F, \tag{10}$$

where V is the volume of the Si NC film under investigation ($L \times 10\ \mu\text{m} \times 10\ \mu\text{m}$ for the bulk film and $l \times 10\ \mu\text{m} \times 10\ \mu\text{m}$ for the channel). To be able to compare Γ with the photoinduced charge carrier densities n_{photo} and n^{*}_{photo}, we account for the dependence on the illumination intensity in Eq. (9). As $n_{\text{photo}} \propto I_{\text{photo}}$ and $F \propto \Gamma$, we conclude that $n_{\text{photo}} \propto \Gamma^{\gamma}$ [47]. Consequently, in Fig. 8, Γ^{γ} is plotted as a function of Si NC film thickness, where Figs. 8(a) and 8(b) show the generation rates in the (effective) thickness L and

Figs. 8(c) and 8(d) show the generation rates in the FET channel. The photon flux is adjusted to the values used for the sample series I and for the sample series II. In Figs. 8(a) and 8(b), the generation rate decreases with film thickness, showing only a slightly more pronounced decrease for UV than for red light illumination. In the FET channel, the generation rates significantly differ for larger film thicknesses showing a decrease of 1.5 orders of magnitude under UV and 0.5 orders of magnitude under red light illumination [Figs. 8(c) and 8(d)]. Comparing the simulation results with experimental data in Figs. 4(c) and 4(d) and Figs. 5(c) and 5(d), respectively, we find that the trends are in good agreement with the experimental data. In Figs. 4(c) and 4(d), we observe an average decrease of n_{photo} of 0.5 orders of magnitude with increasing film thickness from 100 to 1000 nm, the simulation data [Figs. 8(a) and 8(b)] show a similar decrease for both UV and red light illumination. Importantly, n_{photo} is more or less independent of the illumination wavelength in the experiment and the simulation. Regarding the FET channel [Figs. 5(c) and 5(d)], n^*_{photo} exhibits similar values at low film thicknesses under UV and red illumination. With increasing thickness, we observe a decrease between 0.5–1 orders of magnitude for red illumination, whereas n^*_{photo} under UV illumination decreases at least 1.5 orders of magnitude. The simulation data [Figs. 8(c) and 8(d)] is in good agreement with the experimental data showing similar values for UV and red illumination at low thicknesses and a much stronger decrease of Γ^γ for UV than for red illumination with increasing thickness. We can conclude that the simulated Γ^γ well represents the trends of the experimental n_{photo} and n^*_{photo}.

For comparison, we also estimate the generation rate considering Eq. (10) and Lambert-Beer's law $P = 1 - \exp(-\alpha L)$, where α is the absorption coefficient [45]. The parameter α is determined from the optical absorption measurements in Fig. 1(g) to be $\alpha(390\text{ nm}) = (10 \pm 5) \times 10^4\text{ cm}^{-1}$ and $\alpha(623\text{ nm}) = (4 \pm 2) \times 10^3\text{ cm}^{-1}$. These generation rates are inserted as dashed lines in Fig. 8. We find that this simple model does not represent well the main characteristics of the numerically computed and the experimental data. In Figs. 8(a) and 8(b), Γ^γ shows similar values for UV and red illumination, which is not the case in the Lambert-Beer model. In Figs. 8(c) and 8(d), the trend of the numerical values is somehow reproduced, however, the similar values at low film thicknesses are again not well represented by the Lambert-Beer model. The main difference between the FDTD numerical simulation and the Lambert-Beer model is the surface morphology of the Si NC films.

In our simulation model, charge carriers that are photogenerated within the rough top layer of the films are not considered for the calculation of the generation rates. In the Lambert-Beer approach, an effective film thickness with a flat surface is used. Therefore, charge carriers generated close to the film surface are considered. The experimental data are in line with the simulation data rather than with the Lambert-Beer model. This suggests that the charge carriers created in the rough top surface of the NC film do not contribute to the charge transport and the top layer is electrically inactive. The surface roughness is, therefore, very important for the photodetection efficiency.

In conclusion, we find that the simulated generation rates (Fig. 8) and measured n_{photo} [Figs. 4(c) and 4(d)] and n^*_{photo} [Figs. 5(c) and 5(d)] show the same dependence on film thickness. The generation rate is computed from optical data resulting in a profile of photogenerated charge carriers. Note that not all these charge carriers do necessarily contribute to the measured photocurrent as the extraction efficiency may depend on the position in the Si NC film. In contrast, in the transport measurements, we observe charge carriers that are actually contributing to the charge transport from source to drain. The generation rates and the photogenerated charge carrier density show the same trend with film thickness, which has been explained using $n_{\text{photo}} \propto \Gamma^\gamma$.

Importantly, this relation only holds if the film is electronically homogeneous and a constant share of the photogenerated electrons is transported through the NC film. If, for example, the charge transport is restricted above a certain film thickness, then n_{photo} would decrease significantly faster than Γ^γ. In our NC films, we find that the generation rates are proportional to the photoinduced charge carrier densities in the whole thickness range. This holds for the bulk and for the channel of the Si NC FETs. Therefore, we can conclude that all layers of the Si NC films are contributing equally to the charge transport and have similar charge transport properties.

We can further assume that, if the electronic properties of the Si NCs in the bulk and the FET channel are similar, then the field effect mobility, which can be measured in the FET channel only, does not change significantly in the bulk of the film. This conclusion is based on a comparison between the experimental photoinduced charge carrier densities and the calculated charge carrier generation rates, as discussed above. Since the trends observed in the experimental and calculated data agree within a factor of 2, we infer that the mobility should be contact within a factor of 2 across the films' thickness. As pointed out above, the assumption of uniform charge transport properties does not hold for the surface of the Si NC film. Here, the rough top surface of the NC films prevent that photogenerated charge carriers are being extracted.

V. CONCLUSION

We have studied the charge transport and optoelectronic properties of NC films. FETs of Si NCs were used to measure electrical conductivity and field effect mobility of NC films with different thicknesses. We extracted the photoinduced charge carrier density in the bulk of the films (n_{photo}) and in the FET channel (n^*_{photo}) using UV and red light illumination. The results were compared with FDTD simulations of charge carrier generation rates. We find that the values of n_{photo} are similar for UV and red illumination and show only a small decrease with film thickness. This is in contrast to n^*_{photo} where under UV illumination, a large decrease with increasing thickness is observed. Comparing the experimental results with FDTD simulations, we conclude that the dependencies of n_{photo} and n^*_{photo} on film thickness are well reproduced using a simple optical model of the NC films. We conclude that the charge transport is homogeneous throughout the NC film and that the rough surface portion of the films is electrically inactive. Although our study has been carried out with Si NC films deposited by means of spray coating, we think that

our conclusions could also be applied to films of other NCs deposited by other methods, provided that the morphology of the films is similar to that of our Si NC films, i.e., that the films are formed by a three-dimensional network of randomly distributed NCs with a roughness that is similar to or larger than the mean diameter of the NCs. Our work points out the importance of achieving a high control over film roughness for the application of NC films in optoelectronic applications requiring the harvesting of strongly absorbed photons.

ACKNOWLEDGMENT

This work has been supported by the Cluster of Excellence Nanosystems Initiative Munich. The work has also been developed in the scope of the project I3N (Project No. UID/CTM/50025/2013), financed by national funds through the Fundação para a Ciência e a Tecnologia/Ministério da Educação e Ciências (FCT/MEC) and when applicable cofinanced by FEDER under the PT2020 Partnership Agreement.

[1] M. V. Kovalenko, L. Manna, A. Cabot, Z. Hens, D. V. Talapin, C. R. Kagan, V. I. Klimov, A. L. Rogach, P. Reiss, D. J. Milliron, P. Guyot-Sionnnest, G. Konstantatos, W. J. Parak, T. Hyeon, B. A. Korgel, C. B. Murray, and W. Heiss, ACS Nano **9**, 1012 (2015).
[2] J. Y. Kim, O. Voznyy, D. Zhitomirsky, and E. H. Sargent, Adv. Mater. **25**, 4986 (2013).
[3] C. R. Kagan, E. Lifshitz, E. H. Sargent, and D. V. Talapin, Science **353**, aac5523 (2016).
[4] D. Vanmaekelbergh and P. Liljeroth, Chem. Soc. Rev. **34**, 299 (2005).
[5] D. J. Norris, A. L. Efros, and S. C. Erwin, Science **319**, 1776 (2008).
[6] D. V. Talapin, J.-S. Lee, M. V. Kovalenko, and E. V. Shevchenko, Chem. Rev. **110**, 389 (2009).
[7] M. G. Panthani and B. A. Korgel, Annu. Rev. Chem. Biomol. Eng. **3**, 287 (2012).
[8] M. Härting, J. Zhang, D. R. Gamota, and D. T. Britton, Appl. Phys. Lett. **94**, 193509 (2009).
[9] H. Sugimoto, M. Fujii, K. Imakita, S. Hayashi, and K. Akamatsu, J. Phys. Chem. C **117**, 6807 (2013).
[10] M. Green, J. Mater. Chem. **20**, 5797 (2010).
[11] U. R. Kortshagen, R. M. Sankaran, R. N. Pereira, S. L. Girshick, J. J. Wu, and E. S. Aydil, Chem. Rev. **116**, 11061 (2016).
[12] F. E. Kruis, H. Fissan, and A. Peled, J. Aerosol Sci. **29**, 511 (1998).
[13] M. T. Swihart, Curr. Opin. Colloid Interface Sci. **8**, 127 (2003).
[14] C. B. Murray, C. R. Kagan, and M. G. Bawendi, Annu. Rev. Mater. Sci. **30**, 545 (2000).
[15] Y. Yin and A. P. Alivisatos, Nature (London) **437**, 664 (2005).
[16] D. Liang, H. Yang, S. W. Finefrock, and Y. Wu, Nano Lett. **12**, 2140 (2012).
[17] R. Lechner, A. R. Stegner, R. N. Pereira, R. Dietmueller, M. S. Brandt, A. Ebbers, M. Trocha, H. Wiggers, and M. Stutzmann, J. Appl. Phys. **104**, 053701 (2008).
[18] P. Guyot-Sionnest, J. Phys. Chem. Lett. **3**, 1169 (2012).
[19] J. P. Clifford, G. Konstantatos, K. W. Johnston, S. Hoogland, L. Levina, and E. H. Sargent, Nat. Nanotechnol. **4**, 40 (2009).
[20] V. Sukhovatkin, S. Hinds, L. Brzozowski, and E. H. Sargent, Science **324**, 1542 (2009).
[21] Z. Deng, K. S. Jeong, and P. Guyot-Sionnest, ACS Nano **8**, 11707 (2014).
[22] J. M. Luther, M. Law, M. C. Beard, Q. Song, M. O. Reese, R. J. Ellingson, and A. J. Nozik, Nano Lett. **8**, 3488 (2008).
[23] M. Schnabel, C. Weiss, P. Löper, P. R. Wilshaw, and S. Janz, Phys. Status Solidi A **212**, 1649 (2015).
[24] O. E. Semonin, J. M. Luther, S. Choi, H.-Y. Chen, J. Gao, A. J. Nozik, and M. C. Beard, Science **334**, 1530 (2011).
[25] I. J. Kramer and E. H. Sargent, ACS Nano **5**, 8506 (2011).
[26] R. W. Crisp, M. G. Panthani, W. L. Rance, J. N. Duenow, P. A. Parilla, R. Callahan, M. S. Dabney, J. J. Berry, D. V. Talapin, and J. M. Luther, ACS Nano **8**, 9063 (2014).
[27] J. Tang, K. W. Kemp, S. Hoogland, K. S. Jeong, H. Liu, L. Levina, M. Furukawa, X. Wang, R. Debnath, D. Cha, K. W. Chou, A. Fischer, A. Amassian, J. B. Asbury, and E. H. Sargent, Nat. Mater. **10**, 765 (2011).
[28] C. J. Stolle, T. B. Harvey, and B. A. Korgel, Curr. Opin. Chem. Eng. **2**, 160 (2013).
[29] G. H. Carey, A. L. Abdelhady, Z. Ning, S. M. Thon, O. M. Bakr, and E. H. Sargent, Chem. Rev. **115**, 12732 (2015).
[30] D.-K. Ko, A. Maurano, S. K. Suh, D. Kim, G. W. Hwang, J. C. Grossman, V. Bulovic, and M. G. Bawendi, ACS Nano **10**, 3382 (2016).
[31] A. K. Rath, M. Bernechea, L. Martinez, F. P. G. de Arquer, J. Osmond, and G. Konstantatos, Nat. Photonics **6**, 529 (2012).
[32] R. Saran and R. J. Curry, Nat. Photonics **10**, 81 (2016).
[33] A. Zabet-Khosousi and A.-A. Dhirani, Chem. Rev. **108**, 4072 (2008).
[34] W. Aigner, M. Wiesinger, H. Wiggers, M. Stutzmann, and R. N. Pereira, Phys. Rev. Appl. **5**, 054017 (2016).
[35] W. H. Evers, J. M. Schins, M. Aerts, A. Kulkarni, P. Capiod, M. Berthe, B. Grandidier, C. Delerue, H. S. van der Zant, C. van Overbeek, J. L. Peters, D. Vanmaekelbergh, and L. D. Siebbeles, Nat. Commun. **6**, 8195 (2015).
[36] M. V. Kovalenko, M. Scheele, and D. V. Talapin, Science **324**, 1417 (2009).
[37] A. P. Kaushik, B. Lukose, and P. Clancy, ACS Nano **8**, 2302 (2014).
[38] J. Knipping, H. Wiggers, B. Rellinghaus, P. Roth, D. Konjhodzic, and C. Meier, J. Nanosci. Nanotechnol. **4**, 1039 (2004).
[39] R. N. Pereira, S. Niesar, W. B. You, A. F. da Cunha, N. Erhard, A. R. Stegner, H. Wiggers, M. G. Willinger, M. Stutzmann, and M. S. Brandt, J. Phys. Chem. C **115**, 20120 (2011).
[40] Lumerical, FDTD solutions available from www.lumerical.com/tcad-products/fdtd/
[41] E. D. Palik, *Handbook of Optical Constants of Solids*, Vol. 1 (Academic, London, 1998).
[42] A. Garahan, L. Pilon, J. Yin, and I. Saxena, J. Appl. Phys. **101**, 014320 (2007).
[43] See Supplemental Material at http://link.aps.org/supplemental/10.1103/PhysRevB.96.035404 for wavelength-dependent

FDTD simulation results and electrical properties of Si NC FETs using a Si_3N_4 dielectric layer.

[44] P. Lampert, and M. A. Mark, *Current Injection in Solids* (Academic, New York, 1970).

[45] S. M. Sze, *Semiconductor Devices, Physics and Technology*, 3rd ed. (Wiley, Hoboken, NJ, 2007).

[46] R. Gresback, N. J. Kramer, Y. Ding, T. Chen, U. R. Kortshagen, and T. Nozaki, ACS Nano **8**, 5650 (2014).

[47] G. Moddel, D. A. Anderson, and W. Paul, Phys. Rev. B **22**, 1918 (1980).

[48] A. Rose, *Concepts in Photoconductivity and Allied Problems* (Interscience, New York, 1963).